



Nanomechanical Characterization of Bone Quality Depending on Tissue Age via Bimodal Atomic Force Microscopy

Jinha Kwon¹ · Hanna Cho¹

Received: 4 May 2023 / Revised: 9 July 2023 / Accepted: 11 July 2023
© The Author(s) 2023

Abstract

Characterization of bone quality during the healing process is crucial for successful implantation procedures and patient comfort. In this study, a bone implant specimen that underwent a 4-week healing period was investigated. Bimodal atomic force microscopy (AFM) was employed to simultaneously obtain the morphology and elastic modulus maps of the newly formed and pre-existing bone regions within the sample. Results indicate that the new bone matrix possessed lower mineralization levels and presented larger, uneven mineral grains, exhibiting the attributes of a woven bone. On the other hand, the old bone matrix exhibited a more uniform and mineralized structure, which is characteristic of lamellar bones. The new bone had a lower overall elastic modulus than the old bone. Bimodal AFM further confirmed that the new bone displayed three regions comprising unmineralized, partially mineralized, and fully matured sections, which indicate a turbulent change in its composition. Meanwhile, the old bone exhibited two sections comprising partially mineralized and matured bone parts, which denote the final phase of mineralization. This study provides valuable insights into the morphological and nanomechanical differences between the old and new bone matrixes and presents a novel approach to investigate bone quality at different phases of the bone-healing process.

Highlights

1. Bimodal atomic force microscopy (AFM) characterized morphology and elasticity at the nanometer scale, with a focus on the tissue age difference between newly formed and pre-existing bone matrixes in a bone implant specimen.
2. The new bone revealed three distinct sections: unmineralized, partially mineralized, and fully matured sections, representing woven bones.
3. The old bone revealed two distinct sections: partially mineralized and fully matured sections, representing lamellar bone.
4. High-resolution AFM can serve as an additional indicator to assess bone quality and integrity.

Keywords Bone quality · Atomic force microscopy · Bimodal AFM · Nanomechanical characterization · Bone tissue age · Woven bone · Lamellar bone

✉ Hanna Cho
cho.867@osu.edu

¹ Department of Mechanical and Aerospace Engineering, The Ohio State University, Columbus, OH 43210, USA

1 Introduction

Bones are a complex and dynamic heterogeneous material with a highly organized structure [1–3]. Bones can rebuild and repair themselves, which follow a well-established sequence of events [4]. For instance, after dental implant placement, the surrounding bone tissue undergoes damage, and bone formation occurs as early as four days postsurgery [5]. Fibroblast-like osteogenic progenitor cells are induced

and differentiate into osteoblasts, which produce osteoid, an early stage of collagen-containing bone matrix; woven bone forms as a result [5–7]. The newly formed woven bone is characterized by its loosely packed and randomly oriented collagen fibril bundles [8–10]. Woven bone plays a crucial role in overall bone formation by providing a scaffold for the synthesis of well-aligned and strong lamellar bones [9–11]. During the 1–3 months of the healing process, the woven bone is replaced by a lamellar bone through a bone remodeling process, in which collagen fibril bundles are aligned and strengthened by mineralization [4, 9]. The microstructure and degree of mineralization of the bone tissue represent the bone quality, which is a key factor for the success of implantation procedures [12–14]. Bone quality during the healing process determines not only implant stability but also the risk of complications, such as peri-implantitis [15]. Moreover, bone quality is closely related to patient comfort and aesthetic outcomes [16, 17]. However, the characterization of bone quality is challenging due to the need for multivariable investigations, such as the assessment of morphological and mechanical properties and high spatial resolution, as the bone-healing and remodeling processes occur at the submicron scale [18–20].

In previous studies, various optics-based techniques and mechanical tests have been employed to investigate bone quality. For example, fluorescent microscopy and micro-computed tomography have been used to quantify newly formed bones and their composition [21–24]; however, these procedures do not directly examine mechanical properties. Traditional mechanical tests, such as compression or tensile test and vibration analysis with piezoceramic transducer, can be performed to investigate the mechanical properties of bone; however, they aim to investigate the implant stability rather than the bone quality itself, but they only provide macro-scale properties [25–28]. On the other hand, nanoindentation (NI) is commonly used to examine bone quality at a smaller scale [29–33]. However, the typical Berkovich indenter tip used in NI limits the lateral resolution to several micrometers, which presents a challenge in linking measured properties with nanoscale morphological information. For a considerably higher resolution, atomic force microscopy (AFM) with a nanometer-scale cantilever tip has been introduced; it provides a morphological map and mechanical properties with nanometer-scale resolution [34–36]. To examine mechanical properties, scholars use the AFM cantilever tip to indent the sample surface, which provides a force-indentation curve similar to that of NI [37–39]. However, the AFM indentation is relatively slow compared with the tapping-mode AFM in obtaining the sample morphology. To address this issue, scientists developed the bimodal AFM, which provides morphological and nanomechanical maps simultaneously with high speed and spatial resolution [40–42].

Although bimodal AFM has been widely utilized to characterize other heterogeneous materials [43–46], studies depicting the nanomechanical properties of bone using this technique are limited. For instance, the bimodal AFM successfully characterized the nanomechanical properties of bone under pathological conditions, which revealed that pathological bones lose their mechanical integrity at the collagen fibrillar scale [47–49]. However, the study only focused on the comparison of pathological bones with healthy bones in mature status. The chronological change of bone's nanomechanical behavior during the natural healing process has not been studied using the bimodal AFM despite its potential for high-spatial-resolution characterization. In addition, the bimodal AFM data were not calibrated accurately in comparison with those of other methods, such as NI.

In this study, we aimed to analyze and compare the bone qualities at two distinct sites, namely the newly formed woven bone matrix and a pre-existing lamellar bone matrix. We used fluorescent microscopy to locate the newly formed bone at the peri-implant site, and bimodal AFM was employed to simultaneously obtain the morphology and elastic modulus maps of the old and new bone matrixes. Furthermore, we conducted NI to calibrate and compare it with our bimodal AFM results. This study provides valuable insights into the morphological and nanomechanical differences between the old and new bone matrixes and presents a novel approach to investigate bone quality in different phases of the bone-healing process.

2 Materials and Methods

2.1 Sample Preparation

The Institutional Animal Care and Use Committee approved the use of animal samples in this study. A dental implant was placed at the second premolar in the mandible of an adult male beagle dog weighing between 10 and 15 kg. To identify newly formed tissue, calcein labels were intravenously injected into the animal before euthanasia. Calcein is a fluorescent dye that selectively binds to calcium ions and incorporates into newly formed bone tissue during mineralization, which results in the formation of fluorescent bands that can be visualized under the microscope [50–52]. The position and presence of these bands can be used to determine the location of newly formed bone tissue. After 4 weeks of post-implantation healing, the implanted premolar construct was obtained. Given that woven bone undergoes rapid development within the initial 4 weeks [5], the sample obtained from the 4-week healing period provided an excellent opportunity to maximize the differentiation between newly formed and pre-existing bone regions. The distinct characteristics of the

healing process were effectively captured during this critical stage. The extracted specimen was fixed in a formalin solution for seven days and embedded in methyl methacrylate resin. To expose the bone and implant interface, the specimen was cut and polished it with 1 μm diamond paste. The specimen was cleaned by sonication in de-ionized water and prepared on a microscope slide for bimodal AFM and NI analysis.

2.2 Bimodal AFM

Bimodal AFM is an advanced AFM technique that utilizes two different modes of the cantilever to simultaneously provide nanoscale topography and mechanical property information [53, 54]. Figure 1a illustrates a schematic of the bimodal AFM technique. The first mode is operated with an AM feedback loop, and the second one is utilized with an FM feedback loop. The amplitude of the first mode was used to generate a topographic map of the specimen, and the frequency of the second mode was employed to obtain an elastic modulus map. In this study, a commercial AFM system (MFP-3D infinity, Asylum Research®) and a cantilever (AC160TS-R3, spring constant 26 N/m, OLYMPUS®) were used. The AM loop was set to the first mode frequency of 288.17 kHz and an amplitude of 2.17 V, and the FM loop was set to the second mode frequency of 1.63 MHz and an

amplitude of 10 mV amplitude. Before scanning the sample of interest, the AFM cantilever was calibrated with a plastic resin that has a similar elastic modulus to the bone. The topographic map of the resin measured by bimodal AFM (Fig. 1b) displayed a smooth surface. Figure 1c, d shows the corresponding elastic modulus map and its histogram, respectively, which revealed a Gaussian distribution with a mean value of 3.8 GPa and a standard deviation of 0.5 GPa. The elasticity of the resin was measured using NI, and a reference value of 3.8 GPa was obtained for calibration of the bimodal AFM parameters (cf. Figure 1e). Figure 1e displays the comparison between the NI and bimodal AFM results. The findings of bimodal AFM displayed a larger distribution than those of NI due to the smaller scale of indentation depth and tip radius. Nonetheless, the bimodal AFM technique offers a remarkably high resolution and speed, which renders it useful for the characterization of small-scale structures. Following the calibration with plastic resin, the AFM tip was promptly used to analyze the morphology and elastic properties of the new and old bone matrixes. Three randomly selected areas with dimensions of 10×10 and $2 \times 2 \mu\text{m}^2$ were scanned in the new bone regions, and three $10 \times 10 \mu\text{m}^2$ areas and two $2 \times 2 \mu\text{m}^2$ areas were scanned in the old bone regions. Each scanning map consisted of 256×256 data points and contained both the height and Young's modulus maps of the samples.

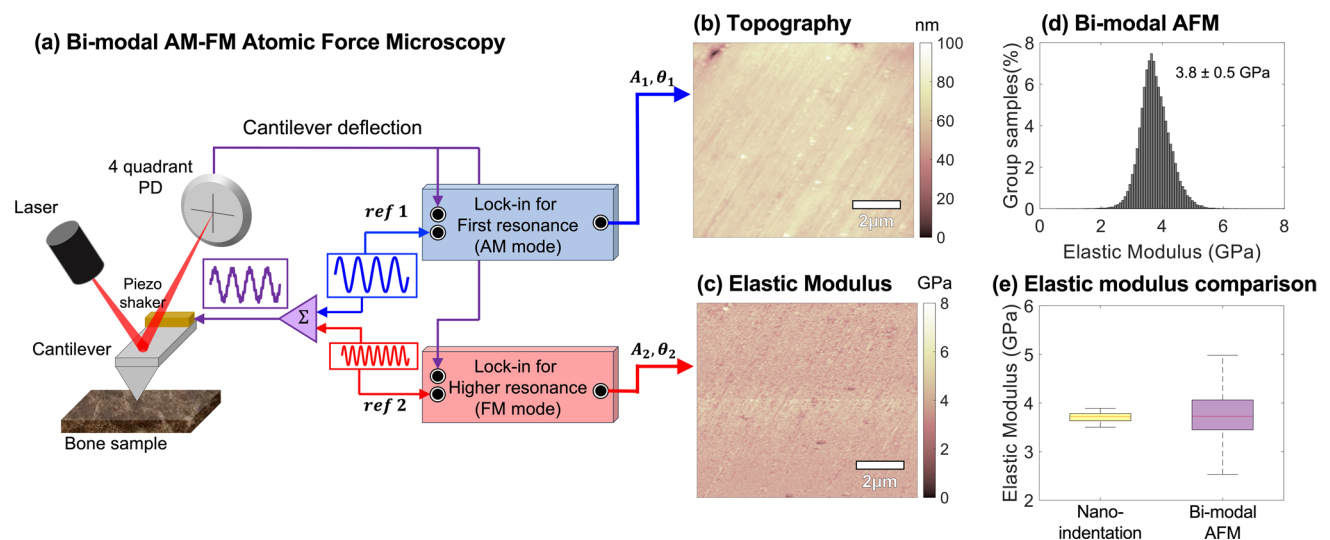


Fig. 1 a Schematic of bimodal amplitude modulation (AM)–frequency modulation (FM) AFM. The cantilever was driven with two simultaneous resonant signals. The topographic information of the specimen was provided by tracking the amplitude of the first resonance (AM mode), and the elasticity of the sample was obtained by tracking the frequency change of the higher mode (FM mode). To

calibrate the bimodal AFM, we obtained the morphology **b** and elasticity map **c** of a plastic resin using the reference value of 3.8 GPa derived from NI. The elastic modulus histogram of the resin **d**, which was measured by bimodal AFM, showed a Gaussian distribution. A comparison between the NI and bimodal AFM results is shown in **e**

2.3 NI

NI is a widely used technique for the measurement of the mechanical properties of thin films or small volumes of materials [29–33]. A Berkovich diamond tip indents the analyzed sample and measures the load–penetration curve. A commercial nanoindenter (Nano Indenter XP, MTS) was employed in this work. The Berkovich tip was calibrated using a fused silica reference sample, which is commonly used for NI calibration. To obtain a reference value to calibrate the bimodal AFM, we examined the Young’s modulus of the plastic resin. A total of 100 points were measured, and the indent points were randomly selected with a separation of 30 microns. The Berkovich tip was indented to 500 nm depth at the rate of 10 nm/s. Following a 30-s hold period, the tip was unloaded at 10 nm/s. By obtaining the unloaded curve, the elastic recovery of the sample was measured and was used to compute the elastic modulus using the conventional Hertzian contact model. To compare the results of bimodal AFM, we also employed NI to measure the new and old bone matrixes. However, given the limited area of the new bone region, only 21 points were measured, whereas 82 points were indented on the old bone region.

3 Result and Discussion

Figure 2a shows the optical image of the bone implant sample, including the metallic implant embedded in the bone matrix. Following the implantation procedure, the surrounding bone matrix was damaged and underwent a healing and remodeling process. After 4 weeks of healing, the gaps between the metallic screws were filled with the new bone matrix. As a result, the new bone matrix was expected to be located near the metallic implant (marked with the red box in Fig. 2a) and the old bone matrix to be further away (marked with the blue box in Fig. 2a). This spatial pattern was confirmed by the fluorescence microscopy images of these areas (Fig. 2b, c). Calcein labeling allowed the identification of newly formed bone tissue, which displayed a strong fluorescent signal under the microscope (Fig. 2b). In addition, the bone matrix far from the implant (Fig. 2c) did not display a strong fluorescent signal. These images indicate the different phases of the bone matrix in the two regions and highlight the successful integration of the implant into the bone matrix.

Figure 3 shows the bimodal AFM maps obtained in the new (red) and old (blue) bone regions. Figure 3a, b, e, f presents the topographic and elastic modulus maps of a $10 \times 10 \mu\text{m}^2$ area, and Fig. 3c, d, g, h displays the corresponding maps of a $2 \times 2 \mu\text{m}^2$ area. AFM measured the cross-sectional structure of the mineralized collagen fibrils, as the sample was cut in a lingual–buccal plane. The

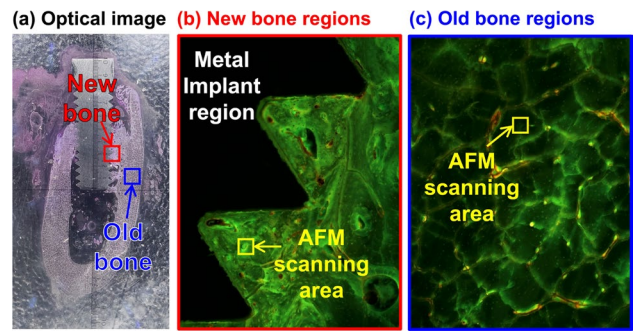


Fig. 2 a Optical micrograph of bone implant sample obtained by loupe ($\times 10$ Magnification). Fluorescence microscopy image of b the new bone regions at the interface of the implant and bone matrix and c the old bone regions far from the metal implant. The yellow boxes in b and c indicate sample locations of the bimodal AFM scanning area. Under fluorescence microscopy, the new bone regions are brighter than the old bone regions because of the calcium labeling, indicating the different phases of the bone matrix

topographic maps revealed that the new and old bones exhibited a grain-like morphology in the cross-sectional structures of their collagen fibrils. Notably, the cross-sectional grains in the new bone matrix were larger than those in the old bone matrix. In addition, the grain size in the new bone varied, whereas the grain size in the old bone was more uniform. This trend persisted across other scanning areas in the new and old bone regions (Supplementary Information). To confirm this observation quantitatively, we identified the grain sizes in the two regions using ImageJ software. Figure 4 shows the filtered outlines of the new bone and old bone grains, which corresponded to the $2 \times 2 \mu\text{m}^2$ topographic maps of the new and old bones in Fig. 3c, g. A total of 75 and 144 grains were detected. As expected, the average area of the grains in the new bone ($0.031 \pm 0.036 \mu\text{m}^2$) was almost twice as large as that in the old bone ($0.016 \pm 0.019 \mu\text{m}^2$), and the standard deviation was also considerably larger in the new bone. This result provides evidence of the difference in the size of mineralized collagen observed between the new and old bone regions.

This difference observed in the grain size between the new and old bone regions indicates a structural change in the bone matrix during the bone-healing process after a dental implant procedure. During a 4-week healing period, woven bone is rapidly formed to fill bone loss sites and subsequently replaced by a well-aligned lamellar bone through the bone remodeling process [4, 5]. Therefore, the new bone matrix was likely predominantly composed of woven bone, and the old bone matrix represented a fully developed lamellar bone. Thus, the variations in grain sizes between the new and old bone regions characterized the mineralized collagen fibrils in the woven and lamellar bone structures. Although further research is necessary to gain a more comprehensive

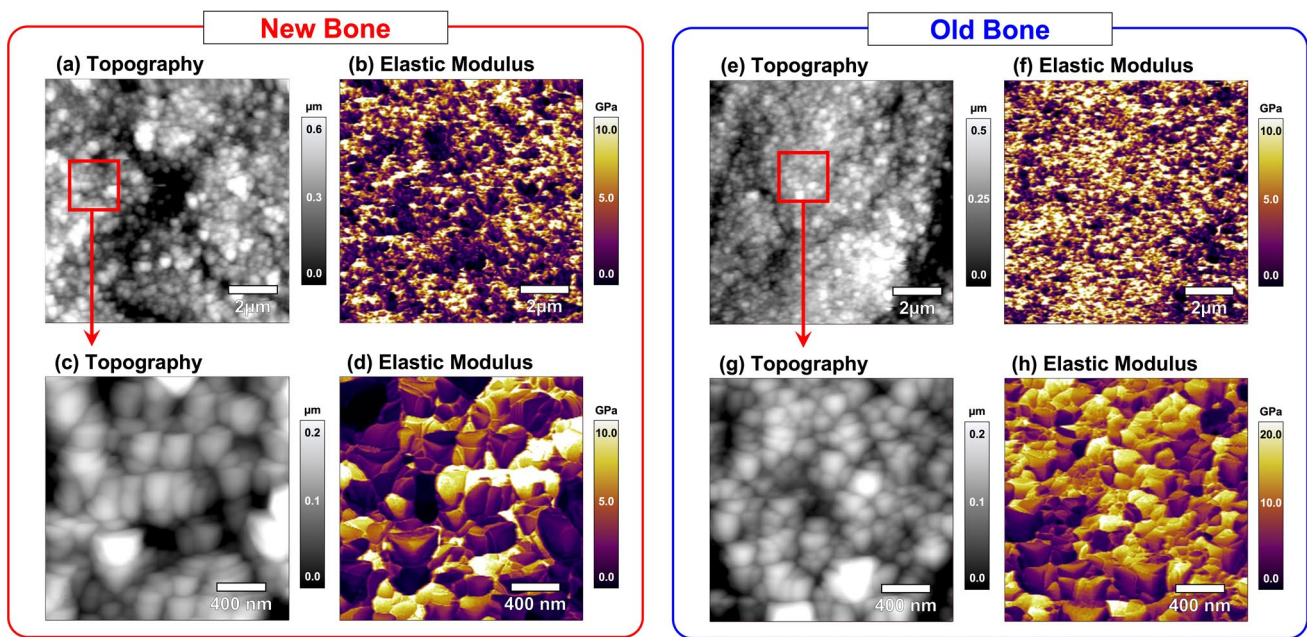


Fig. 3 Morphology and elasticity maps of the bone obtained by bimodal AFM. **a, b** exhibit the topography and elastic modulus maps of a $10 \times 10 \mu\text{m}^2$ area in the new bone region, respectively, and **c**

and **d** display the maps of a $2 \times 2 \mu\text{m}^2$ area. **e, f** show the maps of a $10 \times 10 \mu\text{m}^2$ area in the old bone region, and **g, h** reveal the smaller scale maps of a $2 \times 2 \mu\text{m}^2$ area

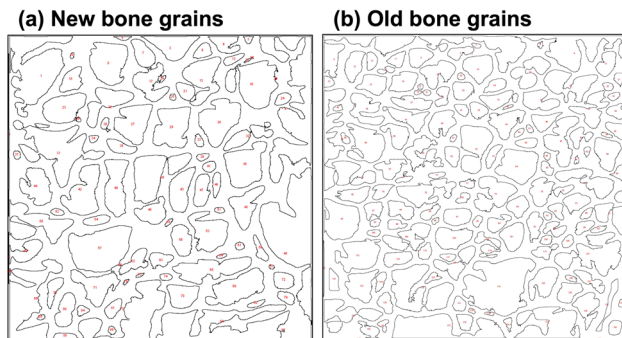


Fig. 4 Outlines of the **a** new bone and **b** old bone particles corresponding to the morphology maps in Fig. 3c, g, respectively. The average areas of mineral grains in the new and old bones were 0.031 ± 0.036 and $0.016 \pm 0.019 \mu\text{m}^2$, respectively

understanding of why woven bone exhibits large collagen fibril sizes, we propose two potential explanations for this observation. First, the larger grain size in the new bone regions can be attributed to oblique sectioning relative to the collagen long axis. In addition, the large distribution of grain sizes in the woven bone may result from the randomly aligned woven bone structure. Conversely, in the lamellar bone, the small and uniform mineral particle size represents the cross-sectional area of well-structured mineralized collagen fibrils. Second, the size difference can be attributed to different mineralization mechanisms in woven and lamellar bones. A single collagen fibril increases its diameter through

intrafibrillar mineralization [55]. However, the precise mineralization mechanism remains unclear, and whether mineralization occurs in the same or different manner in woven bone compared with lamellar bone has not been studied. Considering that collagen serves as a template for mineralization, the different collagen structures between woven and lamellar bones lead to a distinct mineralization process. Thus, misaligned collagen in the woven bone can possibly lead to different ratios of intra-, inter-, and extrafibrillar mineralization, which contribute to the formation of large grain-like structures [18].

In comparison with the elastic modulus maps between the new and old bones, the new bone exhibited a greater heterogeneity than the old bone, which indicates a wider range of elastic moduli. Figure 5 summarizes the elastic modulus data from these maps and NI measurements. For both regions, the data distributions were compared between three different data sets obtained from NI measurements, a $10 \times 10 \mu\text{m}^2$ bimodal AFM map, and a $2 \times 2 \mu\text{m}^2$ bimodal AFM map.

The NI analysis of the new and old bone regions (Fig. 5a, f, respectively) revealed different trends in the elastic modulus depending on the tissue age. The histogram in Fig. 5a shows a relatively uniform distribution of data points across the range of elastic modulus values displayed, which suggests that the bone tissue in the new bone region had a significant amount of variability in its mechanical properties, with no distinct dominant trend. On the other hand, the histogram of NI measurements in the old bone region

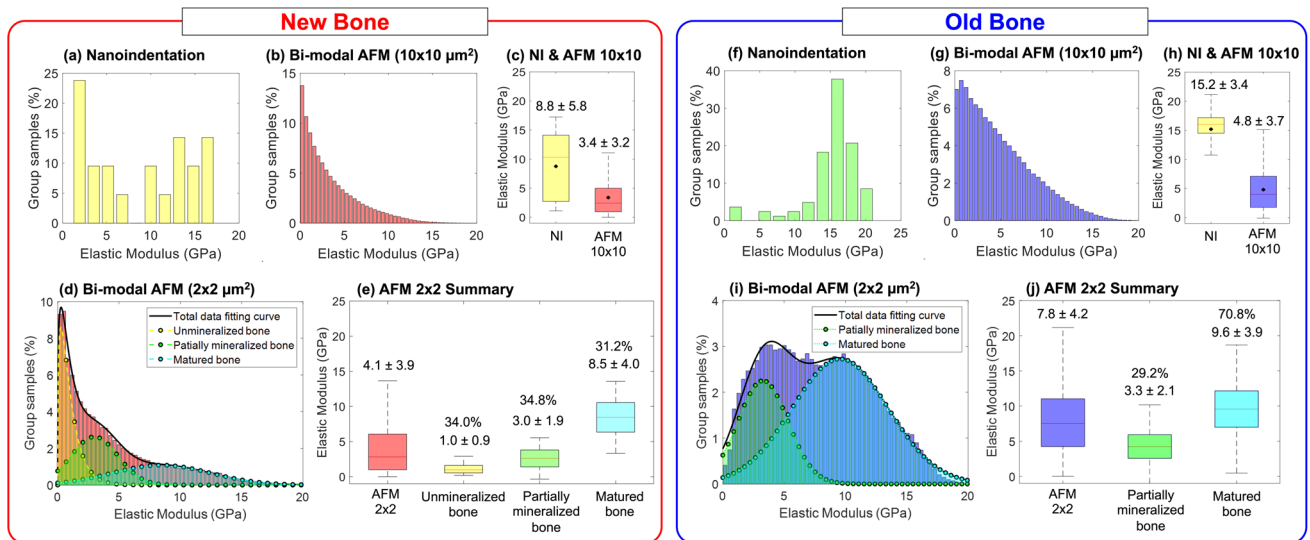


Fig. 5 Elastic modulus results of the new and old bones obtained in NI and bimodal AFM. Histograms **a**, **b** display the elastic modulus distributions of the new bone obtained by NI and bimodal AFM scanning of a $10 \times 10 \mu\text{m}^2$ area, respectively. Boxplot **(c)** compares the elastic modulus obtained using **(a)** NI and **(b)** bimodal AFM. Histogram **(d)** exhibits the elastic modulus measured by the bimodal AFM in a smaller area ($2 \times 2 \mu\text{m}^2$), which revealed three distinct portions of the new bone. The unmineralized bone portion was fitted by a gamma distribution with a yellow line, and the partially mineralized and matured bone portions were fitted by a Gaussian distribution with

(Fig. 5f) showed that the data points were concentrated at higher elastic modulus values with a smaller distribution. This trend is in line with the expected properties of mature lamellar bone, which typically has a uniform and well-defined mechanical behavior. The elastic moduli obtained by NI for the new and old bone regions were 8.8 ± 5.8 and 15.2 ± 3.4 GPa, respectively. Although the NI technique is an effective method for measuring mechanical properties at the micro-scale, its resolution is limited to the accurate examination of mineralized bone structures, which consist of mineral grains that are several hundred nanometers in size, as shown in the bimodal AFM maps in Fig. 3. When the Berkovich tip indents 500 nm in depth, it indents an area of approximately $6.12 \mu\text{m}^2$, which is substantially larger than the size of mineral grains [56]. Therefore, the NI tip cannot distinguish precisely the nanomechanical properties of each bone constituent. Instead, it measured the average elasticity of the indented area. This condition resulted in an overestimation of the elastic modulus obtained by NI. Moreover, the relatively large indentation area required for NI measurements limited the number of data points to 21 for the new bone region and 83 for the old bone region to fit the limited space of the specimen. This sample size was insufficient compared with the 65,536 data points (256 by 256 pixels) obtained in each scanning map of the bimodal AFM. As a result, determining a comprehensive trend of the

nanomechanical properties of the bone solely based on the NI data was challenging. Similarly, histograms **(f)** and **(g)** and boxplot **(h)** show the case of the old bone obtained by NI and bimodal AFM ($10 \times 10 \mu\text{m}^2$). Histogram **(i)** plots the bimodal AFM results ($2 \times 2 \mu\text{m}^2$) of the old bone, in which two Gaussian distributions were fitted to represent the partially mineralized and matured bone portions. Boxplot **(j)** indicates the old bone data averaged over the $2 \times 2 \mu\text{m}^2$ map (blue) and partially mineralized (green) and matured (cyan) portions of the old bone

nanomechanical properties of the bone solely based on the NI data was challenging.

Figure 5b, g displays the elastic modulus histogram obtained by summing the three scanning maps of $10 \times 10 \mu\text{m}^2$ bimodal AFM (additional data shown in Supplementary Information) for the new and old bone regions, respectively. Both histograms exhibit a comparable trend of decreased counts with respect to the elastic modulus. The elastic moduli in the new and old bones were 3.4 ± 3.2 and 4.8 ± 3.7 GPa, respectively, which are notably lower than the values obtained by NI (Fig. 5c, h). Although the bimodal AFM results indicate a higher elastic modulus in the old bone than in the new bone, the distribution was similar between the two regions, which implies that different parts of the mineralized structure could not be distinguished. This result was partly due to the limitation of bimodal AFM techniques and the insufficient spatial resolution of the $10 \times 10 \mu\text{m}^2$ bimodal AFM. The $10 \times 10 \mu\text{m}^2$ scanning area, with 256 by 256 pixels, allowed for a resolution of 39 nm and a measurement area of $1.5 \times 10^{-3} \mu\text{m}^2$. Although these numbers were small compared with the mineral grain size of a few hundred nanometers, the large scanning area compared with the grain size inevitably included a huge number of grains with significant topographic variations, which resulted in data distortion at the edge of each grain.

To address these issues, we scanned $2 \times 2 \mu\text{m}^2$ areas, and their corresponding elastic modulus histograms are shown in Fig. 5d, i. The $2 \times 2 \mu\text{m}^2$ scanning area, with 256 by 256 pixels, allowed for a resolution of 8 nm and a measurement area of $6.1 \times 10^{-5} \mu\text{m}^2$. The new bone histogram data were obtained by combining three scanning maps, and the old bone histogram data were acquired by summing up two scanning maps (Supplementary Information). These smaller-scale maps revealed additional peaks that were not previously visible. The new (Fig. 5d) and old bone data (Fig. 5i) exhibited a multimodal distribution. The distribution of the new bone was successfully fitted using a combination of gamma and two Gaussian distributions, and that of the old bone was fitted using two Gaussian distributions. The mean and standard deviation of each part were determined using the least squares method, and the values are compared in Figs. 5e, j.

As shown in Fig. 5d, the new bone histogram revealed three distinct parts with varying elasticities. The yellow line represents the soft part of the bone, which is likely a pure collagen structure without minerals, and the green and cyan fitted lines denote the partially mineralized and matured bone, respectively. The latter two mineralized portions exhibited a Gaussian distribution. The first soft portion followed a gamma distribution, which can be attributed to the deceleration of the tissue mineralization process. In the new bone region, the unmineralized, partially mineralized, and matured bone parts revealed elastic moduli of 1.0 ± 0.9 , 3.0 ± 1.9 , and 8.5 ± 4.0 GPa, respectively. Each part accounted for a similar portion of the total data set, with values of 34.0%, 34.8%, and 31.2%. By contrast, the old bone histogram in Fig. 5i exhibits two distinct parts regarding elastic modulus but without the unmineralized portion in the new bone matrix. Both parts revealed a Gaussian distribution with elastic moduli of 3.3 ± 2.1 and 9.6 ± 3.9 GPa. Unlike the new bone, the amount of each portion of the old bone was distinct, that is, 29.2% partially mineralized and 70.8% matured bone parts.

The three parts observed in the new bone were consistent with the characteristics of woven bone. Given its high turnover rate, the woven bone is prone to undergo a broad range of mineralization processes, which range from the formation of collagen structure to partially mineralized and fully matured mineralized structure. The absence of an unmineralized portion in the old bone histogram suggests that the bone matrix is not undergoing bone resorption and formation but rather undergoing the final phase of mineralization. This finding is in line with previous studies reporting that the mineralization process occurs in two phases: the first phase that involves the rapid primary mineralization completed in a few months and the second phase that includes the slow secondary mineralization occurring over several years [57, 58]. The comparison of elastic modulus values summarized

in Fig. 5e, j confirmed that the old bone had a higher elastic modulus compared with the new bone when the data were averaged over all parts. However, when comparing the partially and fully mineralized portions, both the new and old bone exhibited similar elastic modulus values. The old bone had a large standard deviation for both portions, which indicated that although the majority of the portions were occupied by the fully mineralized bone, the matured bone maintained a high heterogeneity in terms of nanomechanical properties. The presence of such heterogeneity is a critical quality that allows the bone to maintain strength and toughness, which contribute to its overall fracture resistance. In addition, the similar elastic moduli of the fully mineralized portion in the new bone and that in the old bone suggest that the maximum elastic modulus is attainable after 4 weeks of healing.

Notably, the high-resolution AFM data can provide additional valuable indicators to assess bone quality. The proportions of unmineralized, partially mineralized, and fully mineralized bone parts are critical in defining bone heterogeneity. The presence of each part in specific proportions contributed to the overall mechanical properties of bone, including strength, stiffness, and toughness. The capability to quantify the proportions of each part using high-resolution AFM provides valuable insights into the bone remodeling and mineralization process, which is correlated with tissue age. Moreover, the nanomechanical characterization of distinct mineralization phases, including the value and distribution of elastic modulus, defines not only the mechanical properties but also the level of heterogeneity of each phase. This information can be used as an additional indicator to assess the quality and integrity of bone, which should be important in the diagnosis and treatment of various bone diseases [59–61].

To summarize, the bimodal AFM technique with the high spatial resolution allowed for the identification of different parts of bone based on their mechanical properties. The new bone matrix exhibited three distinct parts, which suggests turbulent changes in the composition during the 4-week healing period. By contrast, the old bone matrix was characterized by two regions with a high elastic modulus, which maintained tissue heterogeneity. However, a few limitations of this study should be considered. First, the bimodal AFM results were affected by contact conditions between the AFM tip and the sample, including the contact angle and surface roughness. This condition can explain the larger elastic modulus distribution observed with bimodal AFM compared with NI (Fig. 1). Therefore, the large distribution of elastic modulus in each sample can be partially attributed to the inherent limitations of bimodal AFM. Second, the effect of collagen misalignment on the elastic modulus of woven bone was not considered, given the difficulty of cutting the sample perpendicular to the direction of collagen fibrils. During mineralization, minerals crystalize and form

apatite nanoplatelets along the collagen fibrillar direction [62–64], which can potentially lead to anisotropic mechanical properties of the bone, depending on the direction of collagen fibrils. Therefore, the wide range of elastic modulus in the woven bone can be partially explained by the misalignment of collagen fibrillar structures. By contrast, the well-aligned lamellar bone, such as the old bone investigated in this study, can be a great platform to investigate the anisotropic properties of bone. For instance, examining the nanomechanical properties of a sample cut in the horizontal plane of the mandible can provide valuable information to understand bone quality for bone implant applications because the mechanical properties in that plane align with the functional loading direction during mastication. Despite these limitations, bimodal AFM remains a powerful tool for simultaneously providing nanoscale information on morphology and mechanical properties. It can aid in the precise evaluation of bone quality by identifying the distinct parts of bone based on their level of mineralization and provide a comprehensive understanding of the structural and compositional changes that occur during the bone-healing process. Furthermore, this method can be used to diagnose other mineralized or pathologically calcified tissues [59–61].

4 Conclusions

In this work, bimodal AFM was employed to characterize the newly formed bone in the vicinity of implantation sites and pre-existing bone far from the sites. The objective was to evaluate bone quality under different tissue ages, which is a crucial factor in determining the stability of the implant system. The newly formed bone matrix was tracked using fluorescent microscopy. Bimodal AFM scanning maps were generated for the new and old bone regions, and differences in their topography and elastic modulus were observed. The new bone matrix was less mineralized and exhibited larger, uneven mineral grains, whereas the old bone matrix displayed a more uniform and mineralized structure. The overall elastic modulus of the new bone was lower than that of the old bone. Further analysis using smaller scanning maps ($2 \times 2 \mu\text{m}^2$) revealed more details regarding the mineralization status of the bone. Specifically, the new bone exhibited unmineralized, partially mineralized, and fully matured portions, and the old bone displayed partially and fully mineralized parts, which indicates that it retained heterogeneity for its material integrity. These findings provide a detailed way to evaluate the extent of mineralization, the amount required for full recovery, and the evaluation of tissue age. The bimodal AFM method is not only suitable for addressing the challenges of characterizing bone quality in implant systems but can also be used to diagnose other mineralized or pathologically calcified tissues.

Supplementary Information The online version contains supplementary material available at <https://doi.org/10.1007/s41871-023-00208-3>.

Acknowledgements We would like to express our gratitude to Dr. Do-Gyoon Kim (College of Dentistry, The Ohio State University) for providing the dental implant sample used in this study.

Author's Contributions The final version of the manuscript has received approval from all authors. All authors have contributed to the study conception and design. Jinha Kwon was responsible for conducting experiments, including material preparation, data collection and analysis, and writing the manuscript. Hanna Cho discussed the contents, reviewed, and revised the manuscript.

Funding This research was partly supported by OSU Material Research Seed Grant and NSF-CMMI-2227527.

Availability of Data and Materials The research data are available upon request to the corresponding author.

Declarations

Conflict of interest The authors declare that they have no conflicts of interest.

Open Access This article is licensed under a Creative Commons Attribution 4.0 International License, which permits use, sharing, adaptation, distribution and reproduction in any medium or format, as long as you give appropriate credit to the original author(s) and the source, provide a link to the Creative Commons licence, and indicate if changes were made. The images or other third party material in this article are included in the article's Creative Commons licence, unless indicated otherwise in a credit line to the material. If material is not included in the article's Creative Commons licence and your intended use is not permitted by statutory regulation or exceeds the permitted use, you will need to obtain permission directly from the copyright holder. To view a copy of this licence, visit <http://creativecommons.org/licenses/by/4.0/>.

References

1. Reznikov N, Shahar R, Weiner S (2014) Three-dimensional structure of human lamellar bone: the presence of two different materials and new insights into the hierarchical organization. *Bone* 59:93–104. <https://doi.org/10.1016/j.bone.2013.10.023>
2. Wegst UGK, Bai H, Saiz E, Tomsia AP, Ritchie RO (2015) Bioinspired structural materials. *Nat Mater* 14:23–36. <https://doi.org/10.1038/nmat4089>
3. Pai S, Kwon J, Liang B, Cho H, Soghrati S (2021) Finite element analysis of the impact of bone nanostructure on its piezoelectric response. *Biomech Model Mechanobiol* 20:1689–1708. <https://doi.org/10.1007/s10237-021-01470-4>
4. Martin RB, Burr DB, Sharkey NA, Fyhrie DP (2015) *Skeletal tissue mechanics*, 2nd edn. Springer, New York
5. Villar CC, Huynh-Ba G, Mills MP, Cochran DL (2011) Wound healing around dental implants. *Endod Top* 25:44–62. <https://doi.org/10.1111/etp.12018>
6. Albrektsson T, Johansson C (2001) Osteoinduction, osteoconduction and osseointegration. *Eur Spine J* 10:S96–S101. <https://doi.org/10.1007/s005860100282>
7. Mavrogenis AF, Dimitriou R, Parvizi J, Babis GC (2009) Biology of implant osseointegration. *J Musculoskelet Neuronal Interact* 9:61–71

8. Reznikov N, Shahar R, Weiner S (2014) Bone hierarchical structure in three dimensions. *Acta Biomater* 10:3815–3826. <https://doi.org/10.1016/j.actbio.2014.05.024>
9. Su X, Sun K, Cui FZ, Landis WJ (2003) Organization of apatite crystals in human woven bone. *Bone* 32:150–162. [https://doi.org/10.1016/S8756-3282\(02\)00945-6](https://doi.org/10.1016/S8756-3282(02)00945-6)
10. Shapiro F, Wu J (2019) Woven bone overview: structural classification based on its integral role in developmental, repair and pathological bone formation throughout vertebrate groups. *Eur Cell Mater* 38:137–167. <https://doi.org/10.22203/eCM.v038a11>
11. Rossi F, Lang NP, De Santis E, Morelli F, Favero G, Botticelli D (2014) Bone-healing pattern at the surface of titanium implants: an experimental study in the dog. *Clin Oral Implants Res* 25:124–131. <https://doi.org/10.1111/clr.12097>
12. Johnson TB, Siderits B, Nye S, Jeong Y-H, Han S-H, Rhyu I-C, Han J-S, Deguchi T, Michael Beck F, Kim D-G (2018) Effect of guided bone regeneration on bone quality surrounding dental implants. *J Biomech*. <https://doi.org/10.1016/j.jbiomech.2018.08.011>
13. Azcarate-Velázquez F, Castillo-Oyagüe R, Oliveros-López L-G, Torres-Lagares D, Martínez-González Á-J, Pérez-Velasco A, Lynch CD, Gutiérrez-Pérez J-L, Serrera-Figallo M-Á (2019) Influence of bone quality on the mechanical interaction between implant and bone: a finite element analysis. *J Dent* 88:103161. <https://doi.org/10.1016/j.jdent.2019.06.008>
14. Lemos CAA, Verri FR, Noritomi PY, Kemmoku DT, de Souza Batista VE, Cruz RS, de Luna Gomes JM, Pellizzer EP (2021) Effect of bone quality and bone loss level around internal and external connection implants: a finite element analysis study. *J Prosthet Dent* 125:137.e1–137.e10. <https://doi.org/10.1016/j.prosdent.2020.06.029>
15. Song X, Li L, Gou H, Xu Y (2020) Impact of implant location on the prevalence of peri-implantitis: a systematic review and meta-analysis. *J Dent* 103490:103. <https://doi.org/10.1016/j.jdent.2020.103490>
16. Esposito M, Grusovin MG, Kwan S, Worthington HV, Coulthard P (2009) Interventions for replacing missing teeth: bone augmentation techniques for dental implant treatment. *Aust Dent J* 54:70–71. <https://doi.org/10.1111/j.1834-7819.2008.01093.x>
17. Liu Y, Bao C, Wismeijer D, Wu G (2015) The physicochemical/biological properties of porous tantalum and the potential surface modification techniques to improve its clinical application in dental implantology. *Mater Sci Eng C* 49:323–329. <https://doi.org/10.1016/j.msec.2015.01.007>
18. Stock SR (2015) The Mineral–Collagen interface in bone. *Calcif Tissue Int* 97:262–280. <https://doi.org/10.1007/s00223-015-9984-6>
19. Kwon J, Cho H (2020) Piezoelectric heterogeneity in collagen type i fibrils quantitatively characterized by piezoresponse force microscopy. *ACS Biomater Sci Eng* 6:6680–6689. <https://doi.org/10.1021/acsbomaterials.0c01314>
20. Kwon J, Cho H (2022) Collagen piezoelectricity in osteogenesis imperfecta and its role in intrafibrillar mineralization. *Commun Biol* 5:1–10. <https://doi.org/10.1038/s42003-022-04204-z>
21. Nkenke E, Kloss F, Wiltfang J, Schultze-Mosgau S, Radespiel-Tröger M, Loos K, Neukam FW (2002) Histomorphometric and fluorescence microscopic analysis of bone remodelling after installation of implants using an osteotome technique. *Clin Oral Implants Res* 13:595–602. <https://doi.org/10.1034/j.1600-0501.2002.130604.x>
22. Peyrin F (2011) Evaluation of bone scaffolds by micro-CT. *Osteoporos Int* 22:2043–2048. <https://doi.org/10.1007/s00198-011-1609-y>
23. Buytaert J, Goyens J, De Greef D, Aerts P, Dirckx J (2014) Volume shrinkage of bone, brain and muscle tissue in sample preparation for micro-CT and light sheet fluorescence microscopy (LSFM). *Microsc Microanal* 20:1208–1217. <https://doi.org/10.1017/S1431927614001329>
24. Faot F, Chatterjee M, de Camargos GV, Duyck J, Vandamme K (2015) Micro-CT analysis of the rodent jaw bone micro-architecture: a systematic review. *Bone Rep* 2:14–24. <https://doi.org/10.1016/j.bonr.2014.10.005>
25. García-González M, Blasón-González S, García-García I, Lamela-Rey MJ, Fernández-Canteli A, Álvarez-Arenal Á (2020) Optimized planning and evaluation of dental implant fatigue testing: a specific software application. *Biology* 9:372. <https://doi.org/10.3390/biology9110372>
26. Lin S-L, Lee S-Y, Lee L-Y, Chiu W-T, Lin C-T, Huang H-M (2006) Vibrational analysis of mandible trauma: experimental and numerical approaches. *Med Biol Eng Comput* 44:785–792. <https://doi.org/10.1007/s11517-006-0095-4>
27. Gao X, Fraulob M, Haïat G (2019) Biomechanical behaviours of the bone–implant interface: a review. *J R Soc Interface* 16:20190259. <https://doi.org/10.1098/rsif.2019.0259>
28. Mattei L, Di Fonzo M, Marchetti S, Di Puccio F (2021) A quantitative and non-invasive vibrational method to assess bone fracture healing: a clinical case study. *Int Biomech* 8:1–11. <https://doi.org/10.1080/23335432.2021.1874528>
29. Pharr GM (1998) Measurement of mechanical properties by ultra-low load indentation. *Mater Sci Eng A* 253:151–159. [https://doi.org/10.1016/S0921-5093\(98\)00724-2](https://doi.org/10.1016/S0921-5093(98)00724-2)
30. Hoffer CE, Guo XE, Zysset PK, Goldstein SA (2005) An application of nanoindentation technique to measure bone tissue lamellae properties. *J Biomech Eng* 127:1046–1053. <https://doi.org/10.1115/1.2073671>
31. Ebenstein DM, Pruitt LA (2006) Nanoindentation of biological materials. *Nano Today* 1:26–33. [https://doi.org/10.1016/S1748-0132\(06\)70077-9](https://doi.org/10.1016/S1748-0132(06)70077-9)
32. Kim D-G, Huja SS, Lee HR, Tee BC, Hueni S (2010) Relationships of viscosity with contact hardness and modulus of bone matrix measured by nanoindentation. *J Biomech Eng* 132:024502–024502–024505. <https://doi.org/10.1115/1.4000936>
33. Kim D-G, Elias KL (2014) Elastic, viscoelastic, and fracture properties of bone tissue measured by nanoindentation. In: Bhushan B, Luo D, Schricker SR, Sigmund W, Zauscher S (eds) *Handbook of nanomaterials properties*. Springer, Berlin, pp 1321–1341
34. Hassenkam T, Fantner GE, Cutroni JA, Weaver JC, Morse DE, Hansma PK (2004) High-resolution AFM imaging of intact and fractured trabecular bone. *Bone* 35:4–10. <https://doi.org/10.1016/j.bone.2004.02.024>
35. Wallace JM (2012) Applications of atomic force microscopy for the assessment of nanoscale morphological and mechanical properties of bone. *Bone* 50:420–427. <https://doi.org/10.1016/j.bone.2011.11.008>
36. Zhou Y, Du J (2022) Atomic force microscopy (AFM) and its applications to bone-related research. *Prog Biophys Mol Biol* 176:52–66. <https://doi.org/10.1016/j.pbiomolbio.2022.10.002>
37. Asgari M, Abi-Rafeh J, Hendy GN, Pasini D (2019) Material anisotropy and elasticity of cortical and trabecular bone in the adult mouse femur via AFM indentation. *J Mech Behav Biomed Mater* 93:81–92. <https://doi.org/10.1016/j.jmbbm.2019.01.024>
38. Chen X, Hughes R, Mullin N, Hawkins RJ, Holen I, Brown NJ, Hobbs JK (2020) Mechanical heterogeneity in the bone microenvironment as characterized by atomic force microscopy. *Biophys J* 119:502–513. <https://doi.org/10.1016/j.bpj.2020.06.026>
39. Qian T, Chen X, Hang F (2020) Investigation of nanoscale failure behaviour of cortical bone under stress by AFM. *J Mech Behav Biomed Mater* 112:103989. <https://doi.org/10.1016/j.jmbbm.2020.103989>

40. Rodriguez BJ, Callahan C, Kalinin SV, Proksch R (2007) Dual-frequency resonance-tracking atomic force microscopy. *Nanotechnology* 18:475504. <https://doi.org/10.1088/0957-4484/18/47/475504>
41. Lozano JR, Garcia R (2008) Theory of multifrequency atomic force microscopy. *Phys Rev Lett* 100:076102. <https://doi.org/10.1103/PhysRevLett.100.076102>
42. Garcia R, Herruzo ET (2012) The emergence of multifrequency force microscopy. *Nat Nanotechnol* 7:217–226. <https://doi.org/10.1038/nnano.2012.38>
43. Dupont MF, Elbourne A, Mayes E, Latham K (2019) Measuring the mechanical properties of flexible crystals using bi-modal atomic force microscopy. *Phys Chem Chem Phys* 21:20219–20224. <https://doi.org/10.1039/C9CP04542B>
44. Bontempi M, Salamanna F, Capozza R, Visani A, Fini M, Gambardella A (2022) Nanomechanical mapping of hard tissues by atomic force microscopy: an application to cortical bone. *Materials* 15:7512. <https://doi.org/10.3390/ma15217512>
45. Mahani ZN, Tajvidi M (2017) Viscoelastic mapping of spruce-polyurethane bond line area using AM-FM atomic force microscopy. *Int J Adhes Adhes* 79:59–66. <https://doi.org/10.1016/j.ijadhadh.2017.09.005>
46. Al-Rekabi Z, Contera S (2018) Multifrequency AFM reveals lipid membrane mechanical properties and the effect of cholesterol in modulating viscoelasticity. *Proc Natl Acad Sci* 115:2658–2663. <https://doi.org/10.1073/pnas.1719065115>
47. Li T, Chang S-W, Rodriguez-Florez N, Buehler MJ, Shefelbine S, Dao M, Zeng K (2016) Studies of chain substitution caused sub-fibril level differences in stiffness and ultrastructure of wildtype and oim/oim collagen fibers using multifrequency-AFM and molecular modeling. *Biomaterials* 107:15–22. <https://doi.org/10.1016/j.biomaterials.2016.08.038>
48. Puthuchery ZA, Sun Y, Zeng K, Vu LH, Zhang ZW, Lim RZL, Chew NSY, Cove ME (2017) Sepsis Reduces Bone Strength Before Morphologic Changes Are Identifiable. *Crit Care Med* 45:e1254. <https://doi.org/10.1097/CCM.0000000000002732>
49. Sun Y, Vu LH, Chew N, Puthuchery Z, Cove ME, Zeng K (2019) A study of perturbations in structure and elastic modulus of bone microconstituents using bimodal amplitude modulated-frequency modulated atomic force microscopy. *ACS Biomater Sci Eng* 5:478–486. <https://doi.org/10.1021/acsbiomaterials.8b01087>
50. Kim D-G, Huja SS, Tee BC, Larsen PE, Kennedy KS, Chien H-H, Lee JW, Wen HB (2013) Bone ingrowth and initial stability of titanium and porous tantalum dental implants: a pilot canine study. *Implant Dent* 22:399–405. <https://doi.org/10.1097/ID.0b013e31829b17b5>
51. Lee JW, Wen HB, Gubbi P, Romanos GE (2018) New bone formation and trabecular bone microarchitecture of highly porous tantalum compared to titanium implant threads: a pilot canine study. *Clin Oral Implants Res* 29:164–174. <https://doi.org/10.1111/clr.13074>
52. White K, Chalaby R, Lowe G, Berlin J, Glackin C, Olabisi R (2021) Calcein binding to assess mineralization in hydrogel microspheres. *Polymers* 13:2274. <https://doi.org/10.3390/polym13142274>
53. Kocun M, Labuda A, Meinhold W, Revenko I, Proksch R (2017) Fast, high resolution, and wide modulus range nanomechanical mapping with bimodal tapping mode. *ACS Nano* 11:10097–10105. <https://doi.org/10.1021/acsnano.7b04530>
54. Santos S, Lai C-Y, Olukan T, Chiesa M (2017) Multifrequency AFM: from origins to convergence. *Nanoscale* 9:5038–5043. <https://doi.org/10.1039/C7NR00993C>
55. Nudelman F, Pieterse K, George A, Bomans PHH, Friedrich H, Brylka LJ, Hilbers PAJ, de With G, Sommerdijk NAJM (2010) The role of collagen in bone apatite formation in the presence of hydroxyapatite nucleation inhibitors. *Nat Mater* 9:1004–1009. <https://doi.org/10.1038/nmat2875>
56. VanLandingham MR, Villarrubia JS, Guthrie WF, Meyers GF (2001) Nanoindentation of polymers: an overview. *Macromol Symp* 167:15–44. [https://doi.org/10.1002/1521-3900\(200103\)167:1%3c15::AID-MASY15%3e3.0.CO;2-T](https://doi.org/10.1002/1521-3900(200103)167:1%3c15::AID-MASY15%3e3.0.CO;2-T)
57. Roschger P, Paschalis EP, Fratzl P, Klaushofer K (2008) Bone mineralization density distribution in health and disease. *Bone* 42:456–466. <https://doi.org/10.1016/j.bone.2007.10.021>
58. Bala Y, Farlay D, Delmas PD, Meunier PJ, Boivin G (2010) Time sequence of secondary mineralization and microhardness in cortical and cancellous bone from ewes. *Bone* 46:1204–1212. <https://doi.org/10.1016/j.bone.2009.11.032>
59. Tsolaki E, Bertazzo S (2019) Pathological mineralization: the potential of mineralomics. *Materials* 12:3126. <https://doi.org/10.3390/ma12193126>
60. Bourne LE, Wheeler-Jones CP, Orriss IR (2021) Regulation of mineralisation in bone and vascular tissue: a comparative review. *J Endocrinol* 248:R51–R65. <https://doi.org/10.1530/JOE-20-0428>
61. Vidavsky N, Kunitake JAMR, Estroff LA (2021) Multiple pathways for pathological calcification in the human body. *Adv Healthc Mater* 10:2001271. <https://doi.org/10.1002/adhm.202001271>
62. Olszta MJ, Cheng X, Jee SS, Kumar R, Kim Y-Y, Kaufman MJ, Douglas EP, Gower LB (2007) Bone structure and formation: a new perspective. *Mater Sci Eng R Rep* 58:77–116. <https://doi.org/10.1016/j.mser.2007.05.001>
63. Nudelman F, Lausch AJ, Sommerdijk NAJM, Sone ED (2013) In vitro models of collagen biomineralization. *J Struct Biol* 183:258–269. <https://doi.org/10.1016/j.jsb.2013.04.003>
64. He W-X, Rajasekharan AK, Tehrani-Bagha AR, Andersson M (2015) Mesoscopically ordered bone-mimetic nanocomposites. *Adv Mater* 27:2260–2264. <https://doi.org/10.1002/adma.201404926>

Publisher's Note Springer Nature remains neutral with regard to jurisdictional claims in published maps and institutional affiliations.



Jinha Kwon holds a PhD in Mechanical Engineering and a Master of Science in Biomedical Engineering, both earned from the Ohio State University in 2022. Prior to that, he earned his Bachelor of Science and Master's degree in Mechanical Engineering at Hanyang University, South Korea, in 2009 and 2011, respectively. Currently, he works as a postdoctoral researcher at Cornell University. His primary research interests are nanoscale multi-domain characterization using atomic force microscopy

for a range of biomaterial applications, spanning from bone tissue to drug delivery polymers.



Hanna Cho is an associate professor in the Department of Mechanical and Aerospace Engineering at The Ohio State University. She earned BS and MS degrees in Mechanical Engineering from Yonsei University, South Korea, in 2002 and 2004, and a PhD at the University of Illinois at Urbana-Champaign (UIUC) in 2012. Cho's research laboratory, the Micro/Nano Multiphysical Dynamics Laboratory, focuses on (i) exploiting nonlinear characteristics in micro-/

nano-electro-mechanical systems (MEMS/NEMS), (ii) advancing the state-of-the-art AFM (atomic force microscopy) techniques beyond topography for enhanced material characterizations, and (iii) applying AFM and microsystems capabilities to various research areas in bio and energy sciences. She has been recognized with prestigious awards, including the Young Faculty Award and Director's Fellowship from the Defense Advanced Research Projects Agency (DARPA), the C.D. Mote Jr. Early Career Award from the American Society of Mechanical Engineers (ASME), and the OSU COE Lumley Research Award.